

## Supporting Information

### **Enrichment and fractionation of rare earth elements (REEs) in ion-adsorption-type REE deposits: Constraints of an iron (hydr)oxide–clay mineral composite**

XIANGXIAO LIANG <sup>1, 3, \*</sup>, PUQIU WU <sup>1, 3</sup>, GAOLING WEI <sup>2</sup>, YIPING YANG <sup>1</sup>,  
SHICHAO JI <sup>1</sup>, LINGYA MA <sup>1, 3</sup>, JINGWEN ZHOU <sup>1, 3</sup>, WEI TAN <sup>1, 3</sup>, JIANXI  
ZHU <sup>1, 3</sup>, YOSHIO TAKAHASHI <sup>4</sup>

<sup>1</sup> CAS Key Laboratory of Mineralogy and Metallogeny/Guangdong Provincial Key Laboratory of Mineral Physics and Materials, Guangzhou Institute of Geochemistry, Chinese Academy of Sciences, Guangzhou 510640, P.R. China;

<sup>2</sup> National-Regional Joint Engineering Research Center for Soil Pollution Control and Remediation in South China, Guangdong Key Laboratory of Integrated Agro-environmental Pollution Control and Management, Institute of Eco-environmental and Soil Sciences, Guangdong Academy of Sciences, Guangzhou, 510650, P.R. China;

<sup>3</sup> University of Chinese Academy of Sciences, Beijing 100049, P.R. China;

<sup>4</sup> Department of Earth and Planetary Science, Graduate School of Science, The University of Tokyo, 7-3-1, Hongo, Bunkyo-ku, Tokyo 113-0033, Japan.

---

\* Corresponding author. E-mail: liangxl@gig.ac.cn (X.L. LIANG).

**Text S1.** Geologic background of Renju deposit

The Renju REE deposit is located in Renju town, Meizhou city, northeast Guangdong province (Figure. S1), with a current total resource of 20,467 tonnes (t) of REO with an average grade of 0.172 wt. % REOs (Wang and Xu, 2016). The deposit is hosted in the weathering crust of Renju pluton, an early Yanshanian granitoids pluton with outcrop area of 29.3 km<sup>2</sup>. The frequent magmatic activities made the metallogenic rocks mostly produced in the form of small rock strains including Zuxitang, Huangniyu and Shenbei (Chen and Yu, 1994).

The Renju granites consist of biotite granite, granite porphyry and quartz diorite. NE-trending and NW-trending faults are mainly developed in this mining area (Figure S1). A small amount of Quaternary sediments, Cretaceous and Cambrian sediments, and Yanshanian rhyolite porphyry interlining tuff are exposed in Renju area. The Renju regolith-hosted REE deposit is mainly developed in the weathering crust of biotite granites. The distribution of orebody is primarily controlled by the topography of pluton, showing a crescent-shaped lenses with an average thickness of 5.6 m.

**Table S1.** Major element concentration of the studied bulk samples along the weathering profile of the Renju ion-adsorption-type rare earth deposit

Depth (m)	Al <sub>2</sub> O <sub>3</sub> (wt.%)	SiO <sub>2</sub> (wt.%)	Fe <sub>2</sub> O <sub>3</sub> (wt.%)	CaO (wt.%)	MgO (wt.%)	K <sub>2</sub> O (wt.%)	Na <sub>2</sub> O (wt.%)	TiO <sub>2</sub> (wt.%)	P <sub>2</sub> O <sub>5</sub> (wt.%)	MnO (wt.%)	CIA (%)
2	22.08	64.38	3.50	0.01	0.01	0.18	b.d.l.	0.52	b.d.l.	b.d.l.	99.15
6	19.80	70.21	2.16	0.01	0.12	0.53	0.04	0.19	b.d.l.	0.05	97.15
10	16.12	74.30	2.23	0.01	0.08	1.57	0.13	0.23	b.d.l.	0.03	90.41
12	17.28	72.01	1.85	0.01	0.09	1.54	0.11	0.19	b.d.l.	0.06	91.24
16	18.91	67.74	2.24	0.01	0.26	3.57	0.25	0.44	0.01	0.06	83.16
20	15.76	72.62	2.23	0.01	0.13	3.89	0.25	0.21	b.d.l.	0.02	79.16
28	14.00	75.40	1.79	0.01	0.11	4.94	0.31	0.18	b.d.l.	0.02	72.69
36	15.21	75.43	0.59	0.01	0.12	5.00	0.15	0.06	b.d.l.	0.01	74.67
40	14.30	74.93	0.96	0.02	0.15	5.63	0.16	0.12	b.d.l.	0.02	71.11
48	22.04	53.14	10.99	0.04	1.16	3.02	0.02	1.69	0.24	0.16	87.74
55	19.55	54.57	11.83	0.06	1.28	2.61	0.02	1.81	0.28	0.31	87.90
65	17.52	55.70	8.06	4.68	2.78	3.10	2.60	1.38	0.56	0.11	62.80
88 (parent rock)	18.75	57.48	4.83	0.87	5.55	0.07	8.22	0.30	0.04	0.17	67.18
90 (parent rock)	19.19	56.36	6.05	0.49	6.04	0.14	7.70	0.28	0.04	0.19	69.73

Note: CIA =  $\text{Al}_2\text{O}_3 / (\text{Al}_2\text{O}_3 + \text{CaO} + \text{Na}_2\text{O} + \text{K}_2\text{O}) \times 100\%$

b.d.l., below the detection limit.

**Table S2.** Chemical composition of biotite (wt.%)

Elements	SiO <sub>2</sub>	Al <sub>2</sub> O <sub>3</sub>	MgO	Fe <sub>2</sub> O <sub>3</sub>	K <sub>2</sub> O	TiO <sub>2</sub>	Na <sub>2</sub> O	CaO	MnO	LOI
Percentage	37.9	16.5	15.6	15.3	8.8	1.7	0.3	0.3	0.2	1.9

Note: LOI = loss on ignition

**Table S3.** Mössbauer parameters of iron-bearing minerals and their compositions at room-temperature in the fine particle fraction (<2  $\mu\text{m}$ ) along the weathering profile of the Renju ion-adsorption-type rare earth deposit.

depth/m	Fe species	IS/mm s <sup>-1</sup>	QS/mm s <sup>-1</sup>	B <sub>hf</sub> /T	Proportion
2	hematite	0.35	-0.25	50.4	33%
	Fe(III) doublet	0.36	0.56	-	67%
10	hematite	0.41	-0.19	49.0	24%
	Fe(III) doublet	0.37	0.58	-	76%
16	hematite	0.40	-0.24	51.0	19%
	Fe(III) doublet	0.37	0.65	-	81%
28	goethite	0.37	-0.26	31.0	31%
	Fe(III) doublet	0.37	0.61	-	69%
36	goethite	0.37	-0.20	31.4	22%
	Fe(III) doublet	0.36	0.61	-	78%
48	goethite	0.37	-0.21	31.0	24%
	Fe(III) doublet	0.36	0.58	-	76%
55	Fe(III) doublet	0.36	0.65	-	100%
65	Fe(III) doublet	0.37	0.59		91%
	Fe(II) doublet	1.14	2.67		9%

**Table S4.** Mössbauer parameters of iron-bearing minerals and their compositions at 14 K in the fine particle fraction (<2  $\mu\text{m}$ ) along the weathering profile of the Renju ion-adsorption-type rare earth deposit.

depth/m	Fe species	IS/mm s <sup>-1</sup>	QS/mm s <sup>-1</sup>	B <sub>hf</sub> /T	Proportion
2	hematite	0.48	-0.16	50.5	88%
	aluminosilicates-Fe(III)	0.39	0.58	-	7%
	Fe(III)-Fe(II) species	0.80	2.22	-	5%
10	hematite	0.48	-0.19	51.2	72%
	aluminosilicates-Fe(III)	0.37	0.78	-	28%
16	hematite	0.43	-0.24	51.0	81%
	aluminosilicates-Fe(III)	0.35	0.65	-	19%
28	hematite	0.48	-0.25	49.7	53%
	goethite	0.45	-0.27	46.9	25%
	aluminosilicates-Fe(III)	0.38	0.78	-	22%
36	goethite	0.44	-0.20	49.3	57%
	aluminosilicates-Fe(III)	0.37	0.58	-	43%
48	goethite	0.43	-0.26	51.3	77%
	aluminosilicates-Fe(III)	0.37	0.67	-	23%
55	goethite	0.49	-0.24	49.0	67%
	aluminosilicates-Fe(III)	0.43	0.52	-	33%
65	goethite	0.52	-0.32	50.1	44%
	ferrihydrite	0.36	0.04	54.2	8%
	aluminosilicates-Fe(III)	0.44	0.65	-	43%
	aluminosilicates-Fe(II)	1.31	2.27	-	5%

**Table S5.** Mössbauer parameters of iron-bearing minerals and their compositions at 14 K in a sample of Bt-60d.

Sample	Fe species	IS/mm s <sup>-1</sup>	QS/mm s <sup>-1</sup>	B <sub>hf</sub> /T	Proportion
Bt60d	hematite	0.52	-0.19	47.3	37.7%
	goethite	0.48	-0.19	44.9	25.6%
	aluminosilicates- Fe(III)	0.48	0.91	-	36.7%

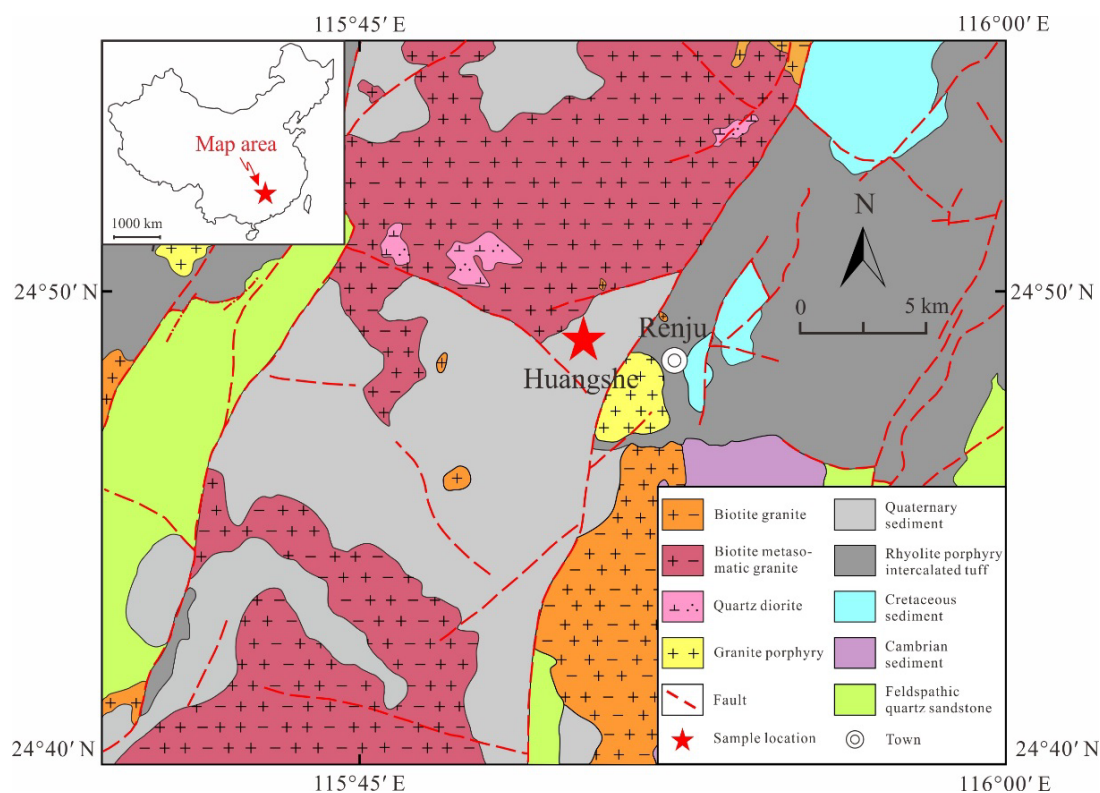


**Figure S1.** Simplified geological map of the Renju ion-adsorption-type rare earth deposit

(Regional Geological Survey Team of Jiangxi Geological Bureau, 1976).



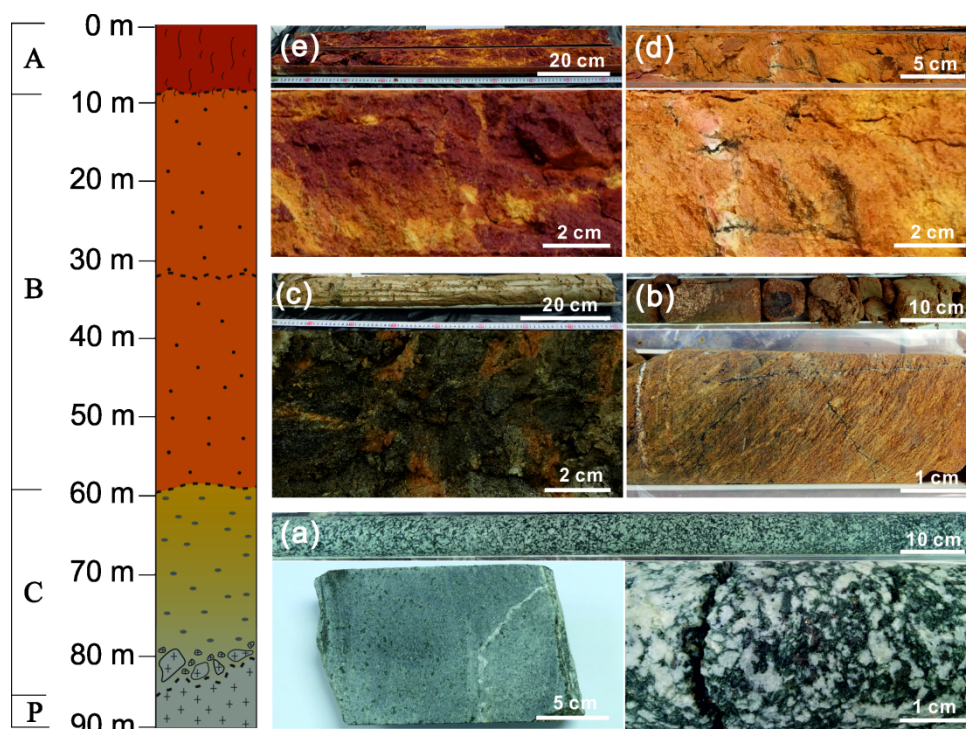


**Figure S2.** Schematic of the weathering profile of the Renju deposit and photographs of the corresponding weathering stages of (a) parent rock (P); (b) semi-weathered horizon (C); (c) lower completely weathered horizon (B); (d) upper completely weathered horizon (B); and (e) top-soil horizon (A).

The bedrock is fine-grained (0.5–2.0 mm) equigranular quartz diorite (Figure S2a), composed mainly of plagioclase, hornblende, quartz, K-feldspar, biotite, and chlorite, where chlorite is the hydrothermal alteration product of amphibole and biotite. REEs are primarily hosted in accessory minerals, which are allanite, titanite, apatite, xenotime, zircon, and monazite with increasing weathering resistance. The C horizon is yellow-green (Figure S2b), owing to extensive chloritisation of biotite and hornblende. The protolith rock is decomposed and fragments are widespread in the weathering fracture. The lower B horizon is a mottled brownish-yellow (Figure S2c). The upper B horizon is less compact and is a mottled red and white, probably due to the heterogeneous distribution of Fe (hydr)oxides in clay mineral aggregates (Figure S2d). Weathered quartz remnants are observed at the macroscopic scale. The A horizon is red and has a loose structure containing a small number of pores (Figure S2e). This horizon is mainly composed of supergene minerals with some rounded residual quartz grains, whereas it contains very little primary feldspar and biotite.

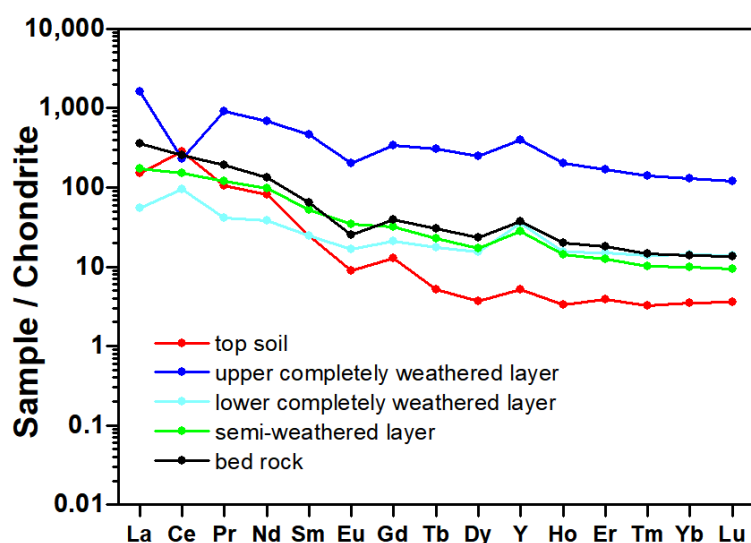


**Figure S3.** Chondrite-normalized rare earth element patterns in top soil (red line), upper completely weathered layer (blue line), lower completely weathered layer (light blue line), semi-weathered layer (green line), and bed rock (black line).

Regarding REE distribution (Figs. 1 and S3), the  $\Sigma$ REE concentration in the bedrock is 496 ppm, markedly higher than the average concentration, i.e.,  $\sim 229$  ppm, in granites in South China. The chondrite-normalized REE pattern is right-inclined with an  $(\text{LREEs}/\text{HREEs})_{\text{N}}$  value of 4.8, indicating that it is enriched in LREEs. In the C horizon, the  $\Sigma$ REE concentration is almost constant (ca. 350 ppm), as are its  $(\text{LREEs}/\text{HREEs})_{\text{N}}$  values (4.0–4.6). As weathering proceeds, the  $\Sigma$ REE concentration clearly increases. In the lower B horizon, there is a high  $\Sigma$ REE concentration (762 ppm) at 50 m. The REE fractionation displays a slight HREE enrichment, as the  $(\text{LREEs}/\text{HREEs})_{\text{N}}$  values are 1.1–2.7, lower than that of bedrock. The  $\Sigma$ REE concentration rapidly increases in the upper B horizon (10–32 m) and reaches a maximum (3343 ppm) at 16 m, ca. 6.6 fold higher than that in the bedrock. In this horizon, there is a substantial accumulation of LREEs, with the  $(\text{LREEs}/\text{HREEs})_{\text{N}}$  values (5.0–17.8) being much larger than that of bedrock (4.8). In the A horizon, the  $\Sigma$ REE concentration is reduced to 350–550 ppm, close to that of parent rock. However, in contrast to bedrock, the REEs in this horizon are dominated by Ce, due to the strongly positive Ce anomaly, resulting in a high  $(\text{LREEs}/\text{HREEs})_{\text{N}}$  value (14.0).

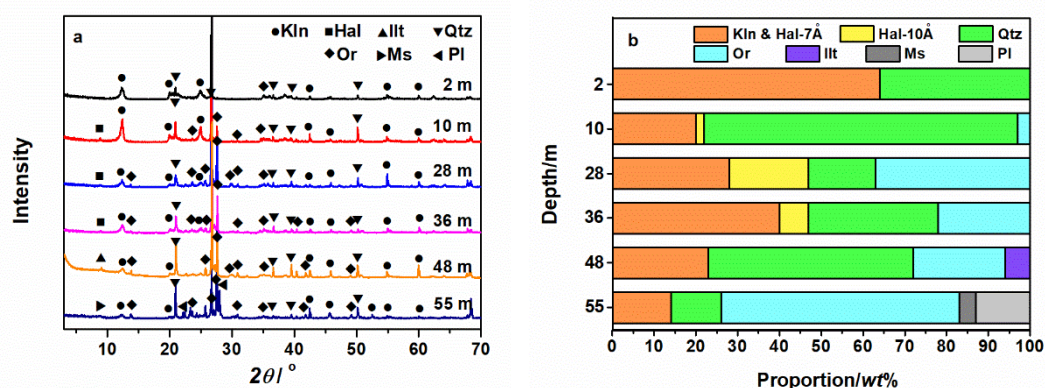


**Figure S4.** X-ray diffraction patterns of the bulk sample (a) and the obtained mineral phase compositions (b) from different soil horizons. Abbreviations: Kln: kaolinite; Hal: halloysite; Qtz: quartz; Or: orthoclase; Ill: illite; Ms: muscovite; Pl: plagioclase.

The variation in mineral phases along the profile of the deposit was analyzed by XRD (Figure S4a). In the entire weathering profile, kaolinite or halloysite-7Å, which are kaolin-group minerals, were identified in the bulk samples based on their characteristic diffractions at ca. 7.17, 4.47 and 3.58 Å, corresponding to (001), (020) and (002) reflections, respectively. In the fine particle fraction, they were further distinguished by the intercalation of formamide. In addition, these clay minerals coexist with quartz and orthoclase at most depths. This is indicated by the characteristic reflections of (100), (101) and (110) of quartz at ca. 4.25, 3.34 and 2.46 Å, respectively, and those of orthoclase, i.e., (002) and (040) reflections at ca. 3.24 and 3.25 Å, respectively. Additionally, there was a weak diffraction at ca. 10.09 Å that, with reference to the TEM observation (see Section 3.1.2), may be attributable to the (001) reflections of halloysite-10 Å at 10, 28, and 36 m, that of illite at 48 m, and that of muscovite at 55 m, consistent with the mineral evolutionary sequence in weathering. Moreover, plagioclase is preserved at the bottom of the B horizon (i.e., 55 m), as verified by the (002) and (-201) reflections at ca. 3.19 and 4.04 Å, respectively, but it is decomposed as weathering proceeds.

The mineral compositions were calculated by the K-value method based on the XRD patterns (Figure S4b). Along the profile of the deposit, kaolinite (or halloysite-7Å), quartz, and orthoclase are the dominant minerals, accounting for more than 70% of the total mineral composition. However, their proportions vary substantially. In the B horizon, the concentration of kaolin-group minerals is mostly less than 30%, but it increases to ca. 70% in the A horizon. However, the concentration of orthoclase, a rock-forming mineral, decreases from 50% at the bottom of the B horizon to less than 5% at the top of the B horizon, due to the decomposition by weathering. In contrast, quartz is a refractory mineral and thus distributed across the entire profile. In general, compared with the A and upper B horizons, the mineral composition in the lower B horizon is more complex. That is, in addition to the three dominant minerals, minor quantities of illite, muscovite, and plagioclase are present. These are rock-forming minerals or intermediate weathering products that are preserved due to weak weathering.

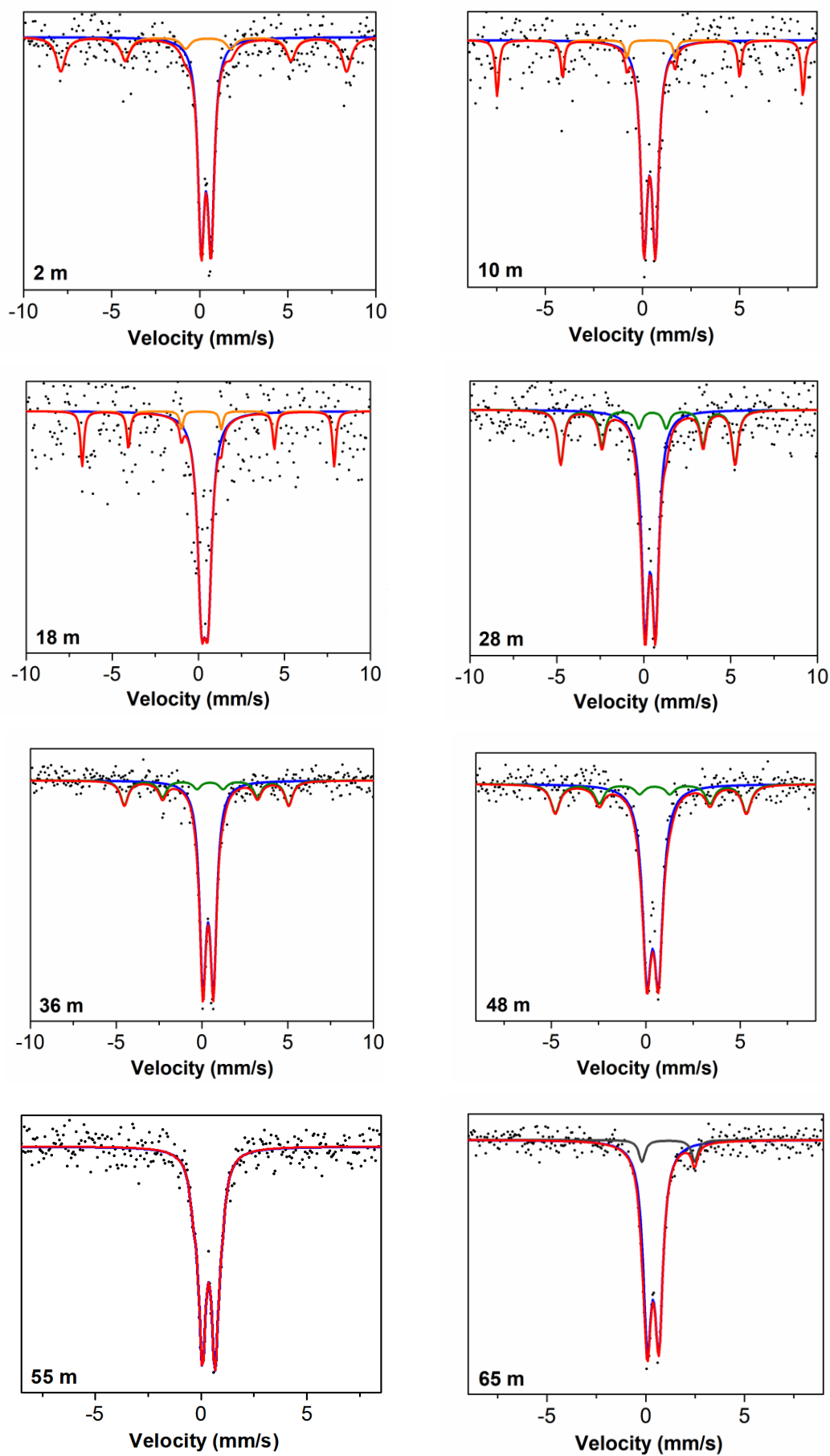


**Figure S5.** Fitted  $^{57}\text{Fe}$  Mössbauer spectra of fine grain ( $<2\ \mu\text{m}$ ) fraction at room temperature. The red solid line is the total calculated fit, through the discrete data points (black solid spots). The resolved spectral components include hematite (orange line), goethite (green line), Fe(III) doublet (I) (blue line), Fe(III) doublet (II) (pink line) and Fe(II) doublet (gray line).

All of the RT spectra consist of a doublet overlapping one or two small sextets. The doublet had an IS value of ca.  $0.36\ \text{mm s}^{-1}$ , consistent with Fe(III)-bearing species, such as Fe(III) in surface-complexes, Fe(III) in aluminosilicates, and Fe(III)-(hydr)oxides that are SP at room temperature. The sextets are attributable to hematite and goethite, as they have similar negative QS values, i.e.,  $-0.19$  to  $-0.25\ \text{mm s}^{-1}$  for hematite and  $-0.20$  to  $-0.26\ \text{mm s}^{-1}$  for goethite. However, the  $B_{\text{hf}}$  of hematite ( $49.0\text{--}51.0\ \text{T}$ ) is larger than that of goethite ( $31.0\text{--}31.4\ \text{T}$ ). Hematite and goethite sextets were present in spectra of samples from region above 16 m and in those from region at 28–48 m, but not in those from region deeper than 48 m. In addition, a doublet with an IS of ca.  $1.14\ \text{mm s}^{-1}$  was in the RT spectra at 65 m, corresponding to an Fe(II)-bearing species.

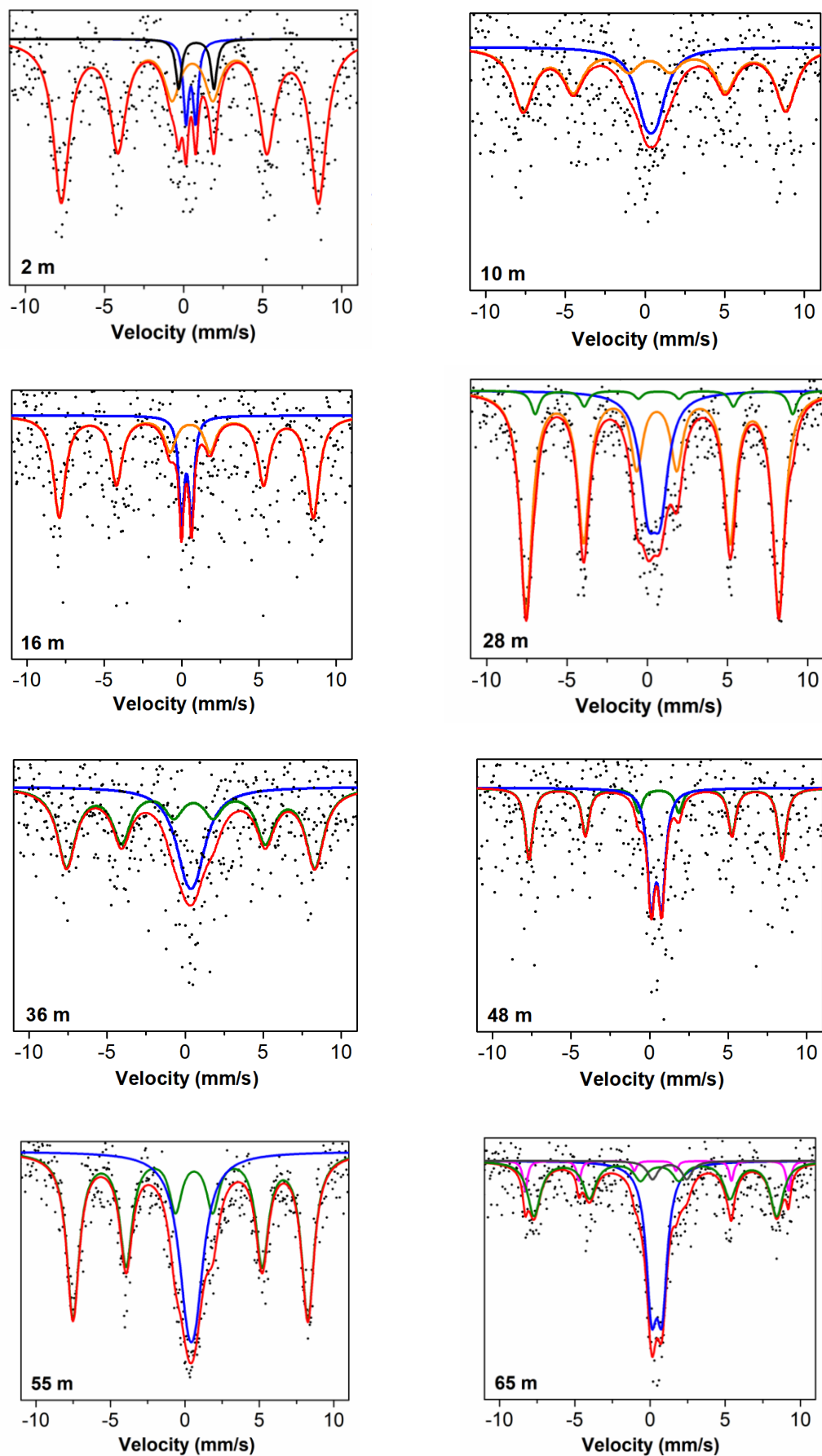




**Figure S6.** Fitted  $^{57}\text{Fe}$  Mössbauer spectra of fine grain fraction ( $<2\ \mu\text{m}$ ) at 14 K. The red solid line is the total calculated fit, through the discrete data points (black solid spots). The resolved spectral components include hematite (orange line), aluminosilicate-iron (III) (Fe(III); blue line), goethite (green line), ferrihydrite (pink line), aluminosilicate-iron (II) (Fe(II); gray line) and Fe(III)-Fe(II) species (dark gray line).

Cooling the samples to 14 K increased the area of the sextets and the doublet, as most Fe(III)-(hydr)oxides became magnetically ordered at this temperature. The Fe(III) sextets showed a clear similarity to those in the spectra of hematite, goethite, and ferrihydrite. The spectra of hematite had an IS of  $0.43\text{--}0.48\ \text{mm s}^{-1}$ , a QS of  $-0.25$  to  $-0.16\ \text{mm s}^{-1}$ , and a  $B_{\text{hf}}$  of  $49.7\text{--}51.2\ \text{T}$  (Figure S6). The IS ( $0.43\text{--}0.52\ \text{mm s}^{-1}$ ) and QS ( $-0.32$  to  $-0.20\ \text{mm s}^{-1}$ ) of goethite are identical to those of hematite, but its  $B_{\text{hf}}$  ( $46.9\text{--}51.3\ \text{T}$ ) is lower than that of hematite. In the spectra of a sample from 28 m, the sextet of ferrihydrite was absent at RT but was present at 14 K, due to magnetic ordering, with an IS of ca.  $0.36\ \text{mm s}^{-1}$ , a QS of ca.  $0.04\ \text{mm s}^{-1}$ , and a  $B_{\text{hf}}$  of ca.  $54.2\ \text{T}$ . At 14 K, most Fe(III)-(hydr)oxides were magnetically ordered, and thus the doublet is ascribable to Fe(III) complexed to OM or present in non-Fe-rich silicates. For example, Fe(III) ions in aluminosilicates are too distant from each other to order magnetically and thus were present as a doublet in a spectrum obtained at 14 K, with an IS of  $0.37\text{--}0.44\ \text{mm s}^{-1}$ , and a QS of  $0.52\text{--}0.78\ \text{mm s}^{-1}$ . Consistent with the RT spectra, Fe(II)-bearing species were detected in a sample from a depth 65 m; they had an IS of ca.  $1.31\ \text{mm s}^{-1}$  and a QS of ca.  $2.27\ \text{mm s}^{-1}$ , and are attributable to a small proportion of Fe(II) (5%) existing within biotite in the semi-weathered layer. In addition, a unique doublet was present in a sample obtained from a depth of 2 m; it had an IS of ca.  $0.80\ \text{mm s}^{-1}$  and a QS of ca.  $2.22\ \text{mm s}^{-1}$ , and is probably associated with Fe(III)-Fe(II) species in surface complexes in the humid soil environment.

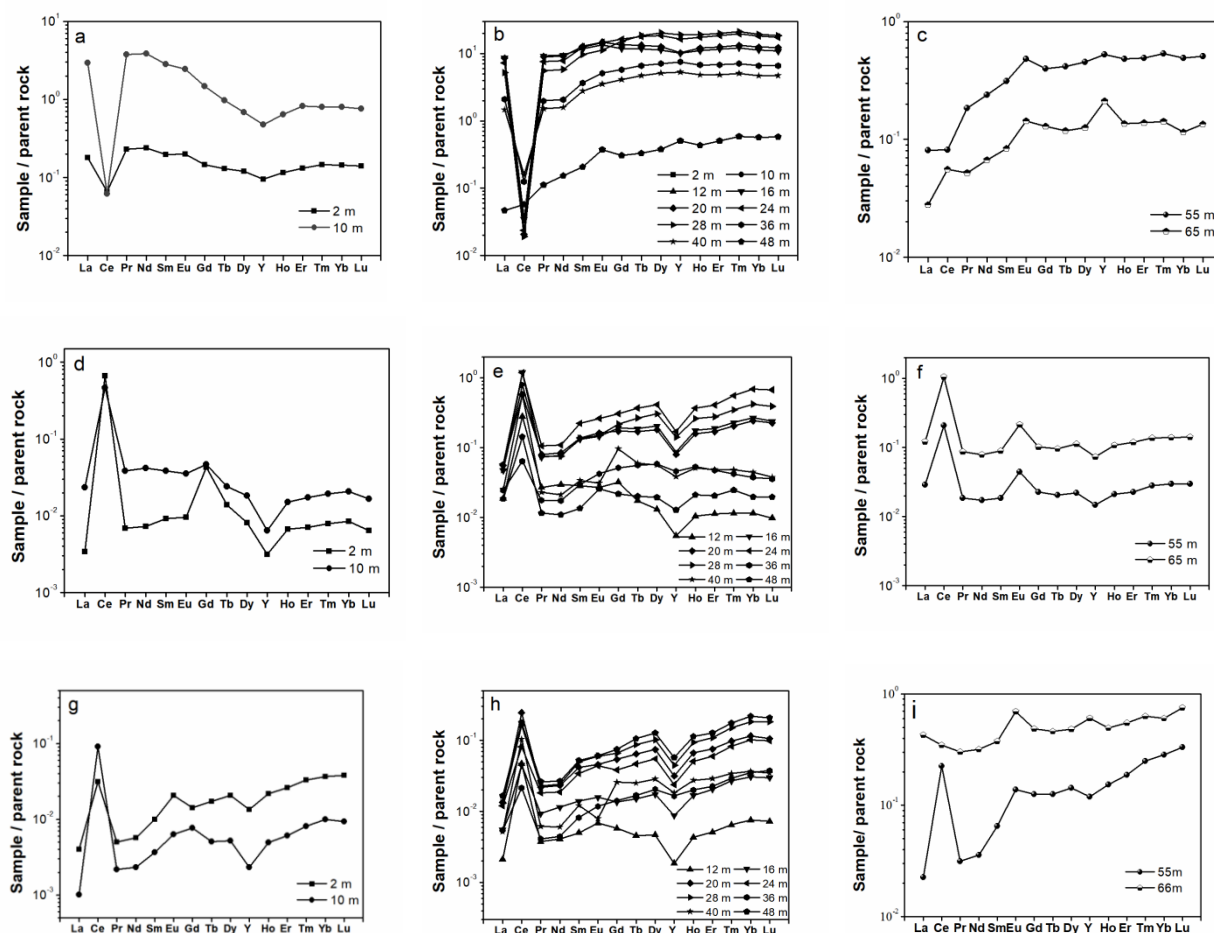


**Figure S7.** Average parent rock-normalized rare earth element concentration profiles with depth in (a, b, c) the ion-exchangeable fraction; (d, e, f) the amorphous iron-manganese (Fe-Mn) oxyhydroxide-associated fraction; and (g, h, i) the crystallized Fe-Mn oxyhydroxide-associated fraction.



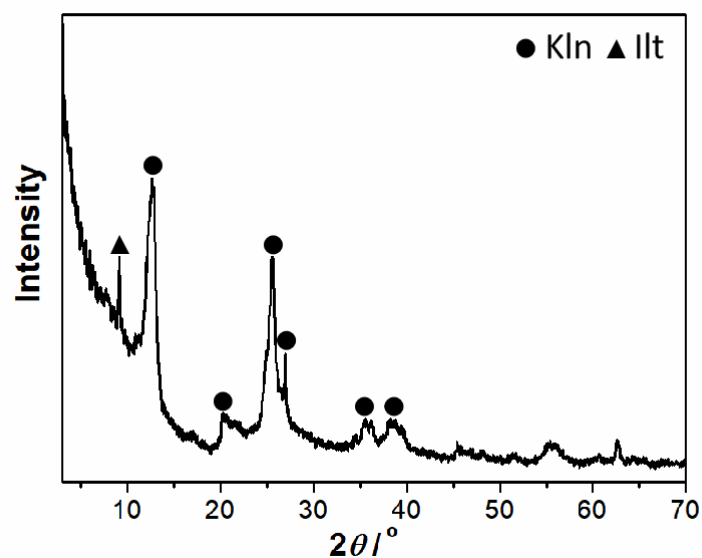


**Figure S8.** X-ray diffraction patterns of a Bt-60d sample.

According to the XRD analysis, kaolinite was the main clay mineral in a Bt-60d sample, accompanied by a small concentration of illite.

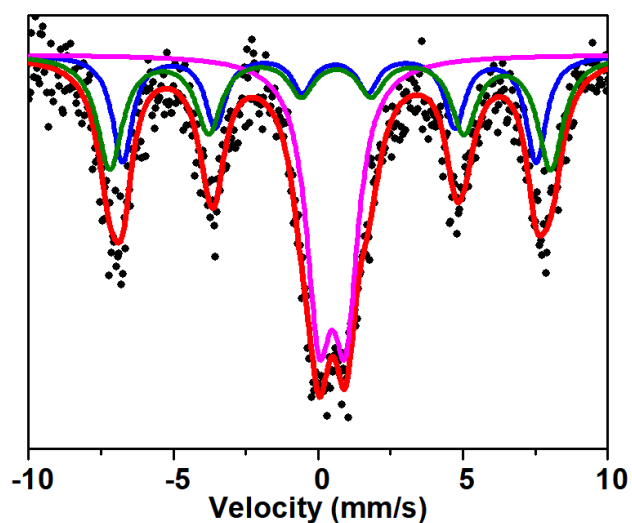


**Figure S9.** Fitted  $^{57}\text{Fe}$  Mössbauer spectra of Fe species in a Bt-60d sample at 14 K. The red solid line is the total calculated fit through the discrete data points (black solid spots). The resolved spectral components include hematite (green line), aluminosilicate–iron (III) species (pink line), and goethite (blue line).

A fitted  $^{57}\text{Fe}$  Mössbauer spectrum at 14 K (Figure S9) and its parameters (Table S3) show that hematite (38%), goethite (26%), and aluminosilicate Fe(III) (36%) were the main Fe-bearing minerals in a Bt-60d sample.

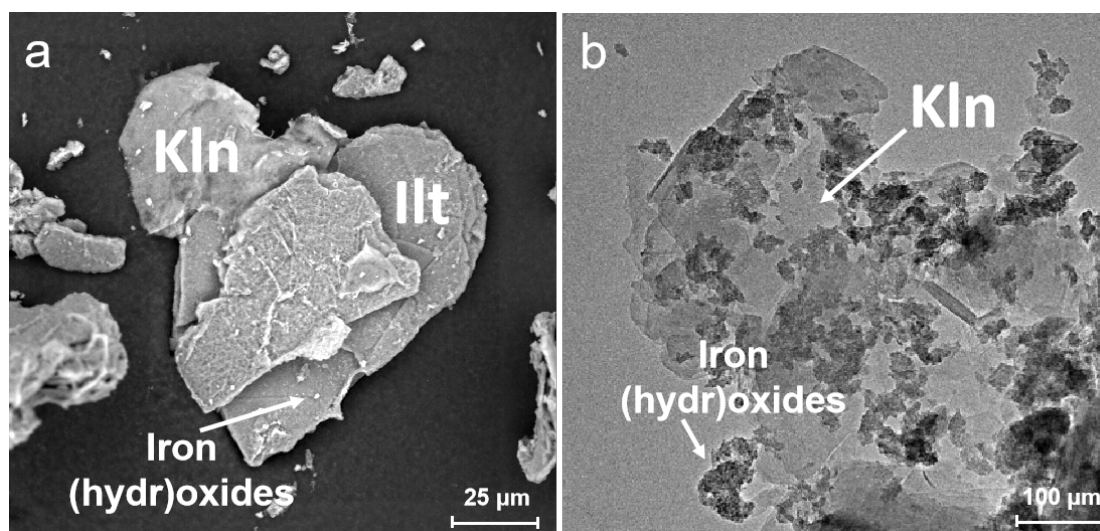


**Figure S10.** Scanning electron microscopy images (a) and transmission electron microscopy images (b) of a Bt-60d sample.

SEM and TEM observations showed that kaolinite, illite, and Fe (hydr)oxides were the main minerals in a Bt-60d sample, consistent with the XRD and Mössbauer results. However, tubular halloysite was not visible in either SEM or TEM images.